Nanoscale

PAPER

View Article Online
View Journal | View Issue

Check for updates

Cite this: *Nanoscale*, 2023, **15**, 8204

Nitrogen adsorption *via* charge transfer on vacancies created during surfactant assisted exfoliation of TiB_2†

Anshul Rasyotra, [a] Anupma Thakur,[a] Raviraj Mandalia,[b] Raghavan Ranganathan[b] and Kabeer Jasuja *[a]

Received 29th November 2022,
Accepted 14th March 2023

DOI: 10.1039/d2nr06676a

rsc.li/nanoscale

Titanium diboride (TiB_2), a layered ceramic material, comprised of titanium atoms sandwiched in between honeycomb planes of boron atoms, exhibits a promising structure to utilize the rich chemistry offered by the synergy of titanium and boron. TiB_2 has been primarily investigated and applied in its bulk form. This perspective is, however, fast evolving with a number of efforts aimed at exfoliating TiB_2. Here, we show that it is possible to delaminate TiB_2 into ultrathin, minimally functionalized nanosheets with the aid of surfactants. These nanosheets exhibit crystalline nature and their chemical analysis reveals vacant sites within the nanosheets. These vacancies facilitate the chemisorption of N_2 onto the TiB_2 nanosheets under ambient conditions without the aid of any energy, this finding was unexpected. This remarkable activity of TiB_2 nanosheets is attributed to vacancies and the Ti–B synergy, which enhance the adsorption and activation of N_2. We obtained supplemental insights into the N_2 adsorption by Density Functional Theory (DFT) studies, which reveal how charge transfer among Ti, B, and N_2 results in N_2 adsorption. The DFT studies also show that nanosheets having more vacancies result in increased adsorption when compared with nanosheets having less vacancies and bulk TiB_2.

Introduction

The last two decades have witnessed extensive research in the domain of two-dimensional (2D) materials. Owing to their high aspect ratio and planar electron confinement, these nanomaterials exhibit properties at the extremes of all known materials. 2D analogs of several van der Waals (vdW) layered materials such as graphite,[1] boron nitride,[2,3] metal dichalcogenides,[4,5] and metal halides[6,7] find wide application. The quest for newer 2D materials has led researchers to also explore non-vdW layered materials wherein planes are held by much stronger forces. This is exemplified by exfoliation of MAX (where M is a transition metal, A is an A group element, and X is C or N) phases,[8,9] oxides/hydroxides of rare earth/transition metals,[10–12] and MAB (where M is a transition metal, A is an A group element, and B is boron) phases.[13,14]

AlB_2-type metal diborides represent one such family of non-vdW layered materials, where boron honeycomb planes are stitched together by metal atoms (see Fig. S1, ESI†).[15] Metal diborides have been investigated and used primarily in their native bulk form. For example, MgB_2 – a flagship member of this family – is known for its superconductivity;[16] TiB_2 is used in ballistic armors;[17] and recently, CoB_2 and MoB_2 have found application in the hydrogen evolution reaction (HER) and nitrogen reduction reaction (NRR).[18,19] The perspective on using metal diborides in their native bulk form has been fast evolving since 2015, when our group reported that it is possible to delaminate MgB_2 into nanosheets using ultrasonication; it was the first report that showcased such feasibility.[20] Since then, several approaches for nanoscaling MgB_2 have been reported: chelation,[21,22] dissolution–recrystallization,[23] cation exchange,[24] interlayer expansion,[25] ultrasonication in ionic liquids/organic solvents,[26,27] and ball-milling.[28,29]

The approaches for nanoscaling MgB_2 are gradually being expanded to other borides, particularly TiB_2, a boride known for its ultrahigh strength, chemical inertness, wear resistance, and good thermal/electrical conductivity.[30] The first such report appeared in 2015, when Pumera and co-workers used an electrochemical path for nanoscaling TiB_2, resulting in its partial exfoliation.[31] A subsequent study, published in 2019, reported successful exfoliation of TiB_2 *via* shear mixing, with nanosheets being heavily oxy-functionalized.[32] In 2020, our group discovered that TiB_2 undergoes dissolution–recrystallization in an aqueous solution of H_2O_2; we used this non-classical recrystallization to develop a scalable approach that results

[a] *Discipline of Chemical Engineering, Indian Institute of Technology Gandhinagar, Palaj, Gandhinagar, Gujarat 382055, India. E-mail: kabeer@iitgn.ac.in*
[b] *Discipline of Materials Engineering, Indian Institute of Technology Gandhinagar, Palaj, Gandhinagar, Gujarat 382055, India*

† Electronic supplementary information (ESI) available. See DOI: **https://doi.org/10.1039/d2nr06676a**

in a high yield of heavily functionalized nanosheets.[33] Although both these approaches successfully converted TiB_2 into its quasi-2D form, the resultant nanosheets were heavily functionalized. While functionalization endowed distinct advantages to these nanosheets,[34–37] it also significantly altered the chemical structure of TiB_2. An approach that preserves the long-range crystallinity of TiB_2 and minimizes functionalization upon nanoscaling would facilitate an enhanced access to the planes of titanium and boron, which is otherwise challenging to achieve. This, in turn, can open unprecedented avenues to utilize the native chemistry of TiB_2, similar to the extraordinary enhancements in catalytic activity embodied by graphene, by virtue of its activated basal planes.[38]

One possible way to minimize functionalization without altering the crystal structure is using organic solvents as the medium of exfoliation. Green and co-workers have recently reported that metal borides can be exfoliated in organic solvents.[27] While this study provides some insights into the degree of functionalization, these are limited. This approach also has two critical challenges – (a) organic solvents are expensive, toxic, and difficult to handle, making their dispersions difficult to process; (b) organic solvents themselves transform into optically active 2D nanostructures during ultrasonication assisted exfoliation.[39] We recently attempted to overcome these challenges by using a co-solvent (isopropanol and water) as the exfoliating medium for TiB_2. While the resultant nanosheets were mildly functionalized, the yield was only ~3%.[40] Thus, there is a need for an approach that exfoliates TiB_2 in high yields without altering the crystal structure.

In this work, we show that TiB_2 can be exfoliated with the aid of sodium cholate in high yield (~25%, a concentration of ~2.5 mg mL^{-1}) with minimal functionalization. The resultant nanosheets are found to be ~6 nm thick and retain the native crystallinity of TiB_2 to a large extent as evidenced by crystallography and elemental composition studies. We also show that varying the surfactant concentration during exfoliation can tailor the stoichiometry of nanosheets from metal-rich to boron-rich. We further show that these nanosheets have inherent capability to chemisorb N_2 without the aid of any energy. Using DFT studies, we obtained mechanistic insights to understand how a synergy of Ti and B atoms and the presence of defects play a simultaneous role in N_2 adsorption over nanosheets. To our knowledge, this is the first report that uses surfactant concentration to tailor the stoichiometry of TiB_2 nanosheets and provide a substrate for N_2 adsorption under ambient conditions. This study is potentially useful for exfoliation of layered ionic solids where surfactant chemistry can help in designing nanosheets with a varying stoichiometry for a plethora of applications.

Experimental section

Synthesis of minimally functionalized TiB_2 nanosheets

We have explained the synthesis protocol under two sections – the first section describes pre-treatment of TiB_2 and the second section describes the use of surfactants to exfoliate treated TiB_2.

(a) Pre-treatment (cleaning) of TiB_2. Briefly, 1 g of TiB_2 (Sigma Aldrich, 99% pure, size <10 μm) was added to 20 mL of deionized (DI) water (Millipore Ultrapure Type – II, ionic conductivity = 18.2 MΩ cm (25 °C)) at a concentration of 50 mg mL^{-1}. The mixture was probe sonicated for 20 minutes at 25% amplitude using a QSonica Q500 probe sonicator. We performed this step to remove any impurities in the parent TiB_2 powder. As explained by Coleman and co-workers, such impurities in parent material could result in additional peaks in optical spectra, which may interfere with results.[41] The procedure for cleaning TiB_2 is schematically represented in Fig. S2, ESI.†

(b) Surfactant-mediated exfoliation of TiB_2. Surfactant solutions with different concentrations (1 g L^{-1} to 5 g L^{-1}) were prepared by adding sodium cholate (Sigma Aldrich, BioXtra ≥99% purity) to 100 mL of DI water and stirring for 10 minutes. Cleaned TiB_2 was added to the surfactant solution and stirred for 10 minutes to obtain a black colored mixture; the color can be attributed to TiB_2. This mixture was then sonicated using a QSonica Q500 probe sonicator with a flat tip for a total run time of 4 hours in 6 s ON/2 s OFF cycles. The temperature was maintained by placing the assembly in an ice bath. After sonication, the mixture was left undisturbed for 30 minutes; solid black sediment was observed at the bottom with a brownish suspension at the top. The top suspension (~$\frac{3}{4}$ of the total volume) was collected and centrifuged at 1500 RPM for 45 minutes at 10 °C. The top $\frac{3}{4}$ volume of the centrifuged sample was collected and studied for the Tyndall effect. It exhibited a distinct path of the laser beam indicating its colloidal nature (Fig. S3, ESI†). This final dispersion was utilized for all further characterization studies. The surfactant was removed by centrifuging the dispersion at 14 500 RPM and dispersing the sediment in DI water. This step was repeated three times before collecting the sediment in a powder form of nanosheets. The detailed steps of removing surfactants and choosing the optimal centrifugation rate are shown in Fig. S4–S8, ESI.†

Structural characterization

The Transmission Electron Microscopy (TEM) and High Resolution-Transmission Electron Microscopy (HR-TEM) images were captured using a Thermoscientific Themis 300 instrument operated at 300 kV. The samples for TEM were prepared as follows: 1 mL of the nanosheet dispersion was diluted 10× with DI water, and 100 μL of this diluted dispersion was drop cast onto lacey carbon Cu grids (Ted Pella, 300 mesh) and dried under ambient conditions. This diluted dispersion was also used to prepare samples for adsorption by Atomic Force Microscopy (AFM) studies by drop casting 10 μL of this dispersion on a freshly cleaved mica substrate (PELCO Ted Pella, 9.9 mm diameter). AFM studies were performed on a Multimode 8-AM (Bruker) operated in the ScanAsyst tapping mode, using a silicon cantilever (spring constant of 0.4 N m^{-1}, resonant frequency of 70 kHz). The powder X-ray diffraction (PXRD) spectra of TiB_2 and nanosheets were obtained using a Bruker D8 instrument equipped with Cu-Kα (1.54 Å) radiation.

Chemical characterization

UV-Vis spectroscopy of the nanosheet dispersions was performed on a Shimadzu UV-1800 spectrophotometer over the range of 200–800 nm using quartz cuvettes (1 cm path length). Dispersions with different concentrations were prepared by a serial dilution of the stock dispersion (concentration of 1 mg mL^{-1}) in DI water. Inductively coupled plasma atomic emission spectroscopy (ICP-AES) studies were performed on a PerkinElmer ICP-AES spectrometer Optima 3300 RL. Ten mL of the diluted nanosheet dispersions were analyzed against Type I DI water (control). The Raman spectra were obtained using a Renishaw Micro Raman spectrometer under 514 nm laser irradiation. Zeta potential measurements were performed using a Malvern Zetasizer Ultra. Folded capillary cells were used for all the measurements, and the temperature was kept constant at 20 °C. X-ray photoelectron spectroscopy (XPS) of the samples was performed on a Thermofisher Scientific Nexsa Base with monochromatic Al-Kα X-ray with energy of 1486.6 eV. TGA and DSC studies were performed on a Simultaneous Thermogravimetric (TG) – Differential Scanning Calorimetry (DSC) analyser (STA 449 F3-Jupiter, NETZSCH Germany). Around 5 mg of the sample was taken in an alumina crucible to measure the adsorption rate of N_2 on TiB_2 nanosheets. Fourier Transform Infrared (FTIR) spectroscopy was performed on a PerkinElmer Spectrum Two spectrometer, operated in the U-ATR mode. Electron paramagnetic resonance (EPR) spectroscopy was performed using a JES – FA200 ESR spectrometer with X-band at room temperature.

Computational methods

The spin polarized calculations presented here were performed in the Vienna *Ab initio* Simulation Package[42–44] (VASP) based on the GGA Perdew–Burke–Ernzerhof exchange–correlation functional.[45] The van der Waals interactions were included by the DFT-D2 method within the Grimme scheme.[46] The energy cutoff for plane wave expansion was set as 600 eV. The convergence criteria for geometric optimization were set as 10^{-9} eV and 10^{-4} eV $Å^{-1}$ for total energy and maximum force, respectively. The Brillouin zone was sampled with an automatic 3 × 3 × 1 grid of *k*-points. The optimized TiB_2 unit cell is used to generate a 3 × 3 × 3 slab structure of TiB_2 with 15 Å vacuum in the [0 0 1] direction. The top 2 layers were unconstrained and were free to interact with the adsorbents whereas the bottom 4 layers were held fixed to their bulk configuration. The optimized unit cell of TiB_2 and the replicated one (3 × 3 × 3 slab) are shown in Fig. S29, ESI.†

The adsorption energies were studied for pristine, monovacant, and divacant TiB_2 for two cases each, namely (i) Ti (0 0 1) exposed and (ii) B (0 0 1) exposed surfaces for N_2 adsorption (Fig. S30, ESI†). The monovacant structures were built by removing one atom at a time from the pristine structure. Considering the symmetry of the top plane, different monovacant and divacant structures were studied. Average adsorption energies were calculated using eqn (1).[19]

$$\Delta E_{*x} = E_t - E_x - E_* \text{ and } \Delta E_{avg\text{-}x} = \Delta E_{*x}/n \quad (1)$$

where, ΔE_{*x} is the adsorption energy, E_t is the total energy of the catalyst with adsorbed species, E_x is the energy of the adsorbed species, E_* is the energy of the catalyst surface, and n is the number of interacting atoms contributing to the active site, here, the top two layers of TiB_2.

Results and discussion

Fig. 1 shows the steps involved in the surfactant-assisted exfoliation of TiB_2. TiB_2 particles (pre-treated, see the Methods)

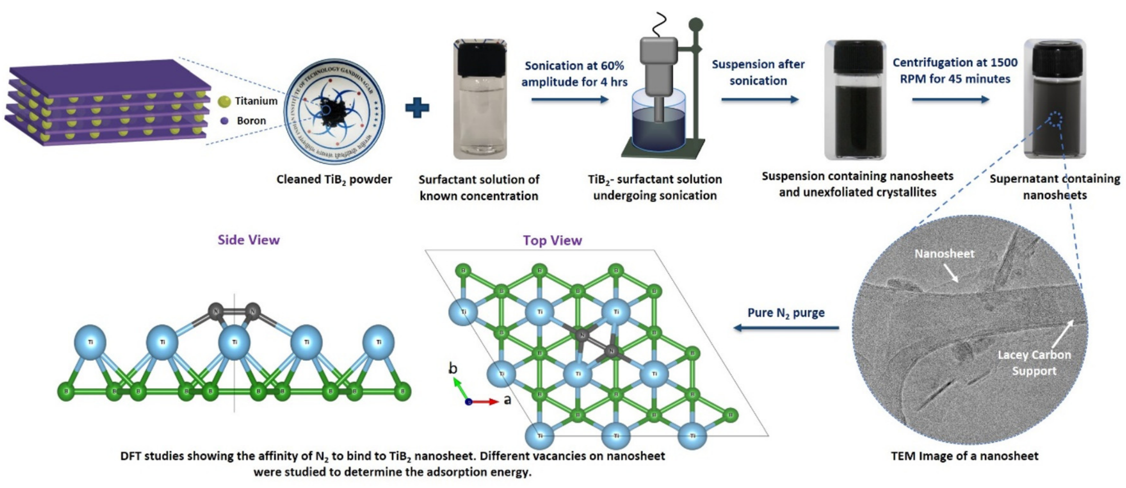

Fig. 1 Surfactant assisted exfoliation route to synthesize minimally functionalized TiB_2 nanosheets. A schematic depicting the surfactant-assisted route to exfoliate TiB_2 with less functionalization. Cleaning *via* probe sonicating TiB_2 powder in a surfactant solution led to a stabilized TiB_2 nanosheet suspension. The suspension was then centrifuged to remove unexfoliated particles. To check N_2 adsorption on minimally functionalized TiB_2 nanosheets, pure N_2 gas was passed through the sample for some time at 25 °C and sample was then heated to 1000 °C to check for an increase in adsorption. DFT results further corroborated the binding affinity of N_2 to nanosheets.

were probe-sonicated for 4 hours in an aqueous solution of sodium cholate, a surfactant widely used in exfoliating layered materials on account of its facial amphiphilicity.[47,48] Sonication resulted in a black colored suspension that was centrifuged at 1500 RPM for 45 minutes to remove macroscopic aggregates. The top brownish supernatant was collected and examined for the Tyndall effect; the presence of a distinct path traced with the laser beam indicated the presence of a dispersed phase in the supernatant (Fig. S3, ESI†).

We analyzed this dispersed phase using transmission electron microscopy (TEM) and observed sheet-like nanostructures. Fig. 2a and b show planar structures with lateral dimensions of ~100 nm–1 µm. We have presented a library of TEM images depicting similar sheet-like nanostructures in the ESI (Fig. S5–S14†). Some nanostructures also displayed Moiré patterns (Fig. 2c); similar patterns were also observed in h-BN nanosheets wherein two layers were tilted with respect to each other by +4°.[49] The presence of such patterns indicates long range crystallinity and lower incidences of functionalization. Furthermore, in our earlier report where we synthesized heavily functionalized TiB_2 nanosheets, we observed wrinkles, folds, and crumples which were attributed to functional groups.[20,21] We do not observe such features in our present study, suggesting that these nanosheets are minimally functio-

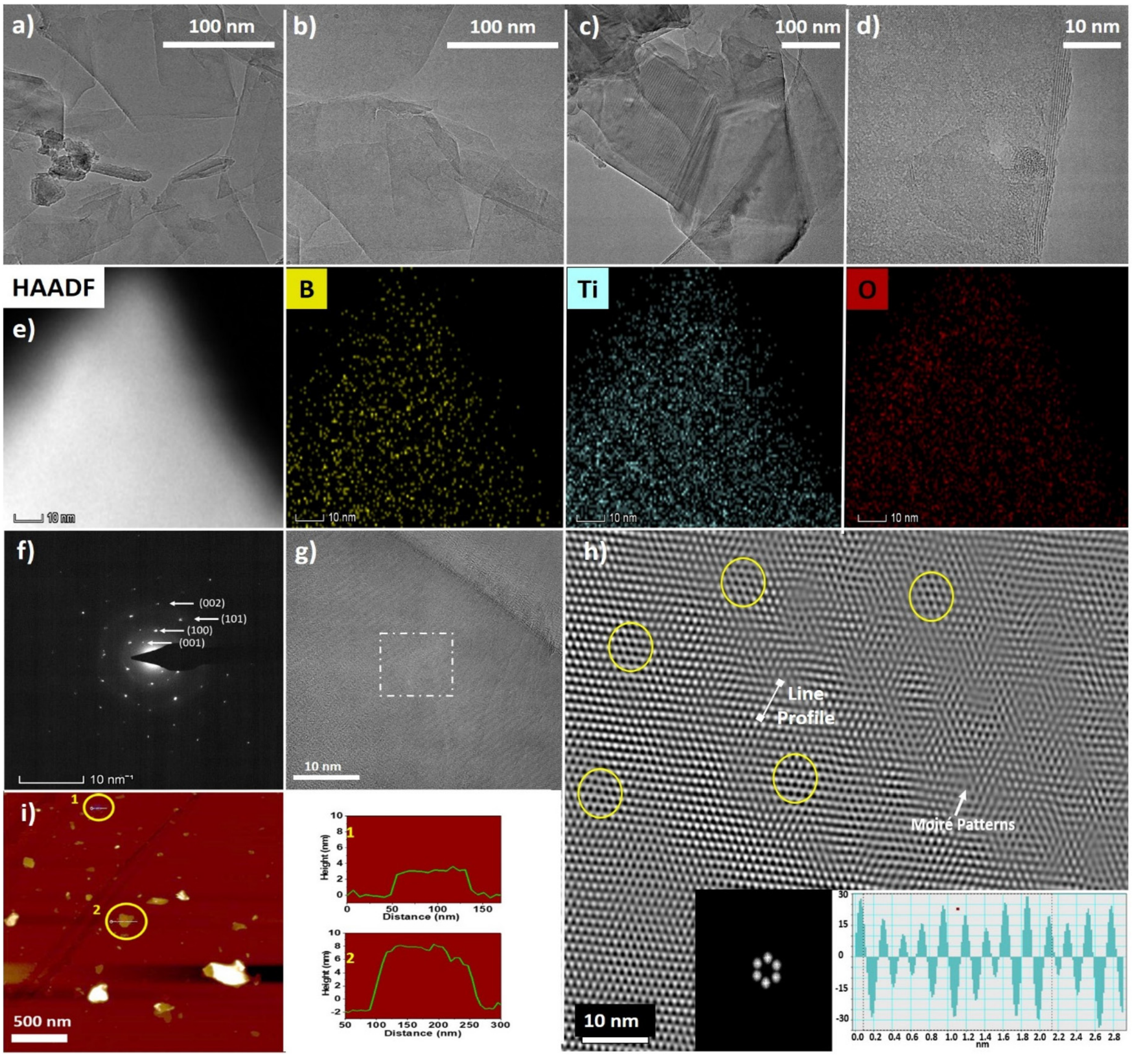

Fig. 2 Microscopic characterization of the nanosheets. (a and b) the TEM images of the nanosheets obtained by drop casting the nanosheet dispersion on lacey carbon grids, (c) Moiré pattern observed in a TEM image of some overlapping nanosheets, (d) the HR-TEM image showing a few layers (~7 layers) on the edge and lattice fringes on the nanosheet basal plane, (e) high-angle annular dark-field (HAADF) combined with scanning transmission electron microscopy-electron dispersive X-ray (STEM-EDX) mapping of a single TiB_2 nanosheet, (f) the SAED pattern obtained shows the polycrystalline nature of the exfoliated nanosheet and superimposed vertices of hexagon indicating the presence of the Moiré pattern, (g) HRTEM image of the nanosheet, and (h) inverse FFT of the selected region of the HRTEM image. Green circles show the hexagonal arrangement, and the inset shows the mask applied and line profile for calculating d-spacing. (i) AFM image, topographical analysis and the corresponding height profile of few nanosheets indicating the thickness of nanosheets to be ~6 nm.

nalized. Fig. 2d presents an HRTEM image showing the transverse view of a nanosheet edge – the alternating dark and light lines indicate few-layer-thick nature of these nanostructures. To obtain information about the chemical composition, we mapped the elements on a sample of the nanosheet. Fig. 2e presents the High-Angle Annular Dark-Field (HAADF) image of the sample nanosheet combined with scanning transmission electron microscopy-electron dispersive X-ray (STEM-EDX) mapping. The mapping shows strong signals of titanium and boron (that are concurrent and uniformly spread) and a weak signal of oxygen indicating minimal functionalization. We have explained about the small degree of oxy-functionalization under the XPS section below. The nanosheets also exhibit a scattered distribution of surfactants on their surface, as captured by sodium mapping (represented in Fig. S15, ESI†). The SAED pattern obtained from these nanosheets exhibits ordered spots (Fig. 2f); we identified that these spots correspond to the (001), (100), (101), and (002) planes of the TiB_2 lattice indicating that crystallinity is retained (the calculations to identify the *hkl* planes from SAED patterns are explained in Table S2, ESI†). To further corroborate these findings, we generated a simulated micrograph of a specific region from the HRTEM image of a nanosheet *via* FFT and inverse FFT (we have outlined these steps in our earlier study).[40] The simulated micrograph displays a long order honeycomb arrangement (Fig. 2h). We generated a line-profile from a region of the simulated micrograph and calculated the *d*-spacing, which was 2.1 Å. This value matches with the *d*-spacing value corresponding to the (101) plane of TiB_2. Although these observations validate the native chemical structure and crystallinity of TiB_2 nanosheets, we observed defects in several TEM images (Fig. S16, ESI†).

We confirmed the quasi-2D nature of these nanosheets using AFM. Fig. 2i shows the area scan and height profiles of two representative nanosheets suggesting that they are few-layer-thick. We measured the thickness of 67 such nanosheets (captured in this frame); a median thickness of 4 nm was observed (histogram shown in Fig. S17, ESI†).

To estimate the concentration of nanosheets in the dispersion, we measured its optical properties. The dispersion shows continuous absorption over the entire UV-visible regime (Fig. 3a) and exhibits a direct band gap of 3.5 eV (calculated

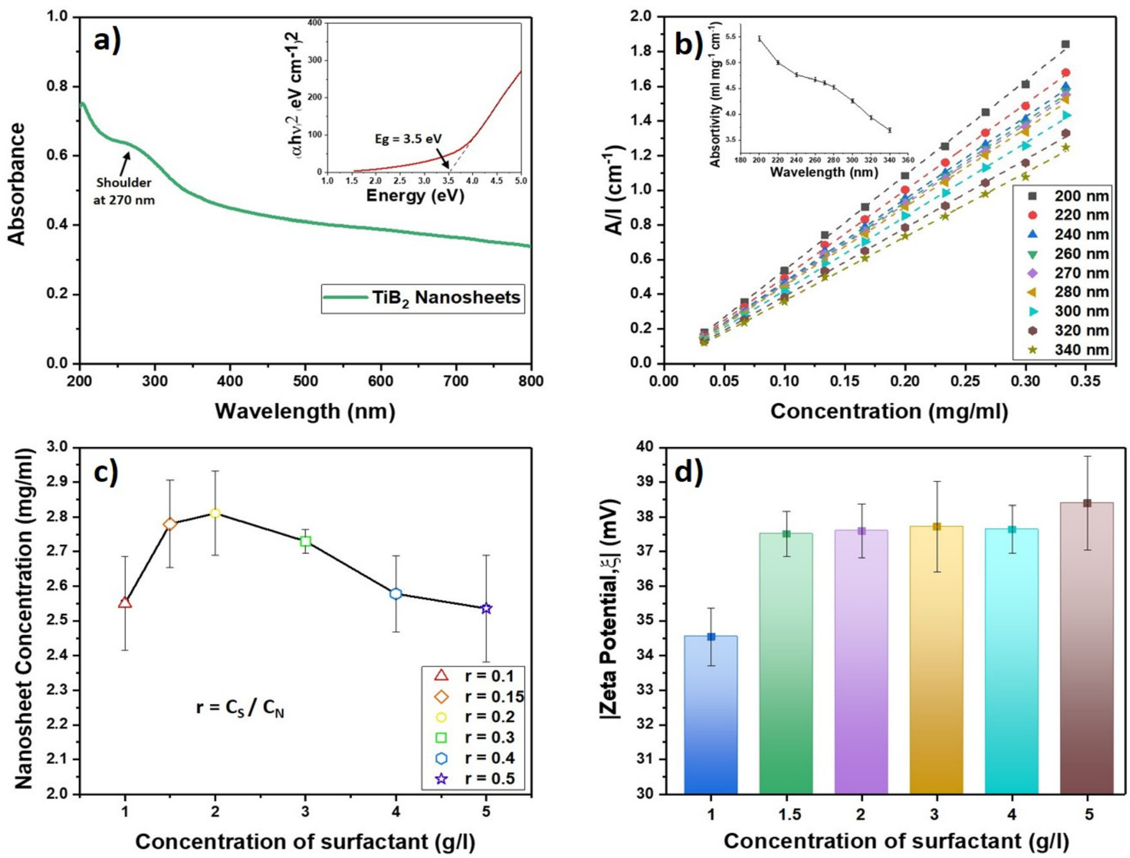

Fig. 3 Optical properties of the colloidal dispersion containing TiB_2 nanosheets. (a) UV-Vis spectra of the synthesized dispersion, showing absorbance in the ultraviolet region with a peak at ~270 nm. The inset graph on the left shows the Tauc plot generated from the absorption spectra of the nanosheet dispersion. The extrapolation of the linear regime in the graph corresponds to a direct band gap of 3.5 eV, (b) estimation of absorptivity of the nanosheet at different wavelengths (R^2 > 0.99, for all cases). The inset graph shows the dependence of absorptivity (decreasing with increasing wavelength) on wavelength, (c) plot of concentration of TiB_2 nanosheets as a function of the sodium cholate concentration in g L^{-1}, and (d) plot of absolute values of the zeta potential measurements *versus* sodium cholate concentration in g L^{-1}.

using the Tauc plot, inset Fig. 3a). The absorption spectra also feature a shoulder at ~270 nm, that is much weaker in intensity compared with the one observed in functionalized MgB_2 and TiB_2 nanosheets, where it was ascribed to the $n \rightarrow \pi^*$ transition (by virtue of oxy-functional groups).[20,33,40] The weak intensity of this shoulder in the present study indicates a much lesser degree of oxy-functionalization (as also observed in the elemental mapping shown in Fig. 2e).

We obtained similar absorption profiles for dispersions with pre-determined concentrations of nanosheets (as explained in Fig. S18, ESI†), and utilized these to generate calibration curves and absorptivity values (Fig. 3b). The absorptivity of these nanosheets decreases with increasing wavelength (inset Fig. 3b), with the maximum value of 5.5 mg^{-1} cm^{-1} mL at 200 nm.[20,35] This value is comparable with that of functionalized TiB_2 nanosheets (ε_{270} = 3.48 mg^{-1} cm^{-1} mL) but an order of magnitude lesser than that of other 2D materials (graphene, WS_2, h-BN, and MoS_2), suggesting that these nanosheets are more transparent than other 2D materials.[20,50–52] To assess how the surfactant concentration (C_S) influences the concentration of nanosheets (C_N), we measured C_N values in final dispersions for C_S values ranging from 1 to 5 g l^{-1}. We observed that C_N increases until C_S = 2 g l^{-1}, and decreases beyond that (Fig. 3c). A similar trend has been observed by Coleman and co-workers in their recent study on the effect of surfactants on WS_2 nanosheets. They attribute the increasing trend to the surfactant's tendency to maximize surface coverage and the decreasing trend to depletion of interactions (preferential flocculation of larger nanosheets).[41] Using zeta potential measurements, we found that the TiB_2 nanosheets are stabilized in the dispersed phase primarily by electrostatic repulsion (Fig. 3d). We observed a negative zeta potential value of ~34 mV, even when C_S = 1 g l^{-1}, highlighting the extremely stable nature of these dispersions.

To confirm whether the above observations on structural and chemical integrity are a representative of the majority of sample, we compared the XRD patterns of nanosheets and bulk TiB_2 and found that they exhibit identical peak positions (Fig. 4a). The XRD pattern of the nanosheets exhibits a reduced intensity and broadened peaks compared with that of bulk TiB_2; this is expected as exfoliation decreases the number of layers in the parent crystal.[53] The nanosheets exhibit a crystallite size of 19.6 nm (calculated using the Scherrer equation for the (101) plane) as compared with a crystallite size of 127 nm exhibited by bulk TiB_2. XRD patterns, previously reported for functionalized and minimally functionalized TiB_2 nanosheets, were always found to exhibit additional peaks (attributed to oxy-functionalization).[33,40] The absence of such additional peaks in the XRD pattern of TiB_2 nanosheets in the present study again evidences the extremely low degree of functionalization. This was also supported by the Raman spectroscopy results. Fig. S19, ESI† compares the Raman spectra of bulk TiB_2 and TiB_2 nanosheets after excitation with a 514 nm laser source. The Raman spectra of bulk TiB_2 is characterized by three peaks at 255 cm^{-1}, 410 cm^{-1}, and 610 cm^{-1} due to the B_{1g}, E_g, and A_{1g} vibration modes.[54,55] The peak in the region of ~550–650 cm^{-1} is attributed to the in-plane, antiphase stretching and hexagon distorting displacement of boron atoms. This peak confirms the presence of B–B bonds in a honeycomb arrangement. Similar peaks were also observed in TiB_2 by Wdowik *et al.*[56] We observed all three peaks in the Raman spectra of nanosheets with a several fold decrease in the intensity. An interesting point to note is that no apparent shift is observed in the peaks compared to those of bulk TiB_2. This decrease in the intensity with no peak shifting indicates the successful exfoliation of TiB_2 to a nanoscale form and the retention of its structure and crystallinity. A similar change in h-BN was observed by Gorbachev and co-workers, where they found a direct relationship between a decrease in the intensity of the Raman spectra and a decrease in the number of layers.[49]

To understand the chemical interface offered by TiB_2 nanosheets, we collected XPS data. The Ti 2p spectra of TiB_2 nanosheets exhibit four peaks centered at 453.7 eV, 457.5 eV, 458.4 eV and 464.2 eV (Fig. 4b). The peak at 453.7 eV corresponds to the Ti–B bond, characteristic of metal borides.[57] When compared with bulk TiB_2 (Fig. S20, ESI†), this peak has a lower intensity and is slightly left shifted. The decrease in the intensity can be explained by a loss of interlayer Ti atoms described as follows. Cavitation induced stress waves and microjets during ultrasonication are known to generate normal and shear forces.[58,59] These forces, when acting upon TiB_2 crystals, are expected to result in a preferential loss of Ti atoms because $E_{Ti-Ti} < E_{Ti-B} < E_{B-B}$ (where E indicates bond energy).[60,61] This preferential loss of Ti atoms is evidenced by ICP-AES studies on nanosheet dispersions (Table S3, ESI†). ICP-AES data for nanosheets prepared at different values of C_S are summarized in Table S3, ESI.† This loss of interlayer Ti atoms also explains the possible origin of the observed exfoliation. This was also corroborated by the TEM images, where vacancies were observed in the form of a line (Fig. S16†). The atomic percentage of the Ti–B bond also decreased from 7.35% (in bulk TiB_2) to 1.03% (in TiB_2 nanosheets) and from 16.11% (in bulk TiB_2) to 5.20% (in TiB_2 nanosheets) in Ti 2p and B 1s spectra, respectively.

We further performed EPR spectroscopy to record the paramagnetic signal to confirm defects (Fig. S22, ESI†). We observed a characteristic S-shaped signal at a calculated *g*-factor of ~2 and an increase in the intensity of this signal at this point for TiB_2 nanosheets. These results indicated that the nanosheets exfoliated were defect-rich. It is pertinent to note that although TEM, XPS and EPR studies confirm the presence of defects, these defects are created in the form of both Ti and B vacancies. Li *et al.* reported the formation of defects in layered metal diborides and XBenes. They presented the possibility of multiple thermodynamically and kinetically favoured configurations that could result from the loss of metal atoms or within the boron honeycombs.[62,63]

We also observed that different surfactant concentrations help to retain different stoichiometries of nanosheets ranging from boron-rich to titanium-rich. This is an unanticipated result, as the prevalent approaches used to exfoliate metal diborides result in either boron-rich nanosheets or metal-rich nanosheets. Surfactant mediated synthesis paves a way to

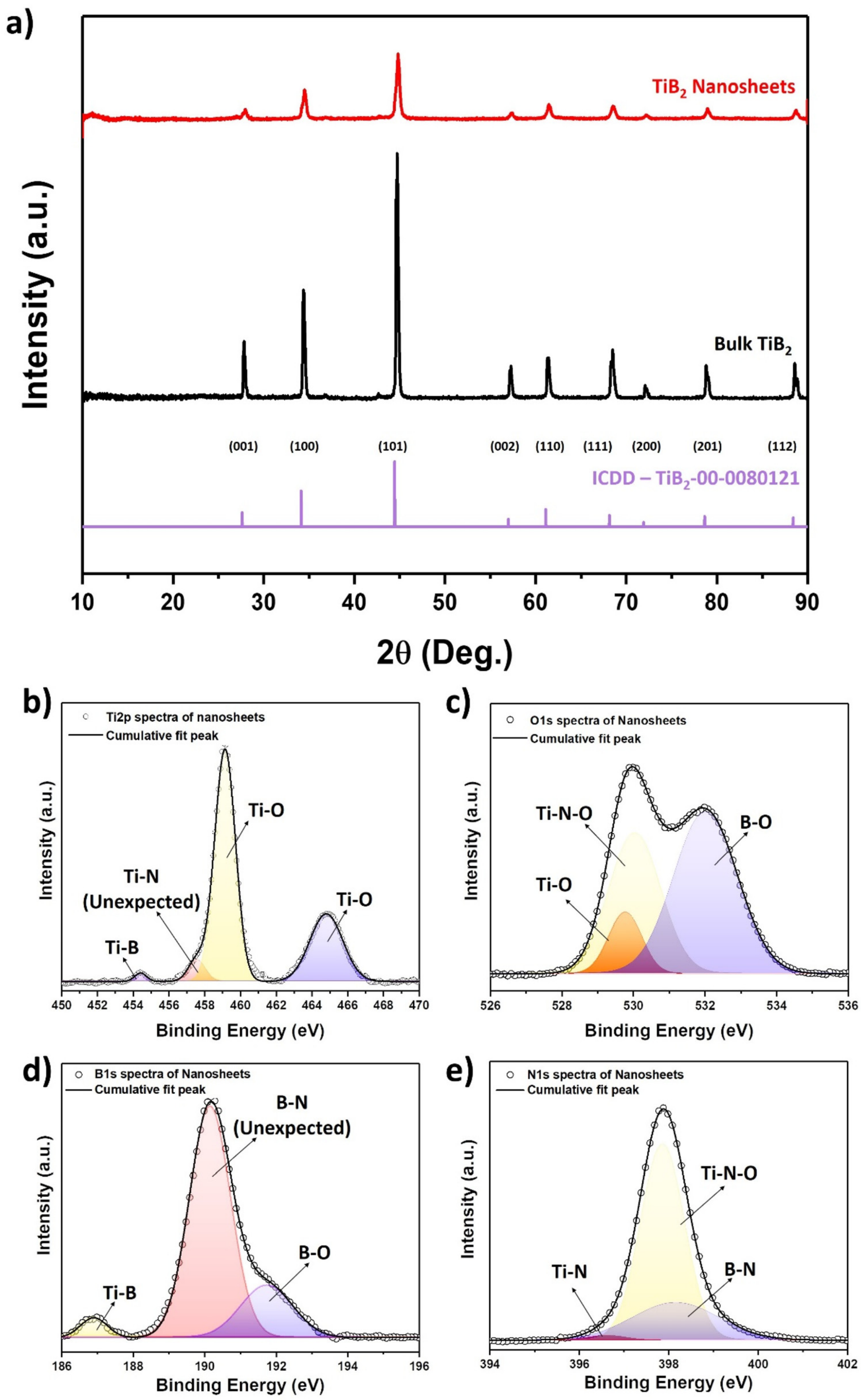

Fig. 4 Chemical characterization of TiB_2 nanosheets. (a) XRD spectra of bulk TiB_2 and TiB_2 nanosheets show similar peaks at varying intensities. The decrease in the intensity along with similar peak positions indicates the retained crystal structure after nanoscaling. XRD spectra of TiB_2 from the standard ICDD data are also plotted. (b) Ti 2p spectra shows the presence of inherent TiB_2 bonding along with the presence of minimal oxy-functional groups, (c) O 1s spectra corroborates the bonding of oxygen with Ti and B, and (d) B 1s spectra of TiB_2 nanosheets shows two expected peaks and one unexpected peak at 190.1 eV. (e) the N 1s spectra of TiB_2 nanosheets shows the presence of both Ti–N and B–N bonds. These spectra were acquired by X-ray photoelectron spectroscopy.

tailor metal atoms and synthesize nanosheets in stoichiometries based upon desired applications while retaining the inherent crystal structure. The number of metal vacancies also alters the electronic band structure in transition metal diborides, thus altering their properties substantially.[64]

The vacant sites, formed as a result of Ti deficiency, can either remain in the form of electron deficient sites/defects,[65] or be compensated by oxy-functionalization, both of which are expected to enhance the catalytic nature. Oxygenated species are known to be induced on the nanosheet lattice due to defects generated during ultrasonication.[66,67] The presence of such electron rich groups on the surface also explains the left shift that we observe in the Ti–B peak and the two peaks in the Ti 2p spectra at 458.4 eV and 464.2 eV, that are ascribed to the $2p_{3/2}$ mode and the $2p_{1/2}$ mode, corresponding to oxy-functionalized Ti (Ti^{4+}).[68] While the Ti 2p spectra provided insights that were expected, we did not anticipate the peak at 457.5 eV. The peak at 457.5 eV correspond to the presence of Ti–N bonds[57,69] on the surface of nanosheets – this is unexpected as N_2 was not involved in synthesis. This unintentional discovery led us to obtain more insights about the fate of N_2 adsorption on TiB_2 nanosheets – we have explained this aspect in depth in a later section.

The O 1s spectra of TiB_2 nanosheets exhibit three primary peaks at 529.7 eV, 530.4 eV and 532 eV. The peaks at 529.7 eV and 532 eV correspond to oxy-functionalized forms of Ti and B, respectively (Fig. 4c).[33] The peak at 530.4 eV is attributed to titanium oxynitride, which was corroborated by the Ti 2p spectra.

The B 1s spectra of TiB_2 nanosheets exhibit three peaks at 187.4 eV, 190.1 eV, and 191.7 eV compared to two peaks observed in bulk TiB_2 (Fig. S20a, ESI†). The peaks at 187.4 eV and 191.7 eV correspond to the Ti–B bond and the B–O, bond respectively – these are expected.[21,68,70] The peak at 190.1 eV corresponds to the presence of B–N bonds[57] on the surface of nanosheets – this is again unexpected. We also observed an N 1s peak in the survey spectra of TiB_2 nanosheets and a faint peak in bulk TiB_2 (Fig. S21, ESI†). The presence of N_2 bonded to both Ti and B led us to consider the counter intuitive possibility of N_2 chemisorbing on the surface of nanosheets. This was also supported by a study where the role of nitrogen was studied during oxidation of TiB_2 leading to the formation of TiN and BN.[71]

To confirm the chemical state of bonded N_2, we further collected the N 1s spectra of nanosheets. The N 1s spectra of nanosheets exhibit three peaks at 396.5 eV, 397.7 eV, and 398.3 eV (Fig. 4e). The peak at 396.5 eV is attributed to the Ti–N bonds, whereas the peak at 397.6 eV corresponds to oxidized TiN – this is also the peak with the highest intensity.[72–76] The third peak at 398.3 eV is attributed to the B–N bonds – this peak is absent in the N 1s spectra of bulk TiB_2 (Fig. S20, ESI†).[77,78] Similarly, the peak of B–N observed in the B 1s spectra of TiB_2 nanosheets was absent in the B 1s spectra of bulk TiB_2. This insinuates the propensity of TiB_2 to chemisorb N_2 at Ti or B sites when nanoscaled to its quasi-2D form.

To obtain some preliminary insights, we studied whether the weight of TiB_2 (bulk and nanosheets) changes when exposed to N_2 inside a TGA chamber – the increase in the mass of nanosheets would validate the adsorption of N_2. We purged ultrapure N_2 at 20 ml min^{-1} to exclude any possibility of other gases interacting with nanosheets. To account for the functionalization that we observed under ambient conditions, we maintained a temperature of 25 °C for the first 15 minutes. We observed a mass increase of 16.8% in TiB_2 nanosheets indicating that nanosheets had inherent capability to adsorb N_2 without the aid of any energy (Fig. 5a and Fig. S24, ESI†). Bulk TiB_2, on the other hand, did not exhibit any mass change under the identical conditions. We then further increased the temperature to 1000 °C to study if the TiB_2 nanosheets would continue to adsorb N_2 at higher temperatures. When the temperature was further increased to 1000 °C, we observed a 46% mass increase in the TiB_2 nanosheets indicating the increased adsorption of N_2 over the surface. We also observed a color change in nanosheets from black to orange (Fig. 5b). In addition, we observed a minor decrease in mass between 250 and 450 °C. This is attributed to increased degradation of residual sodium cholate present in the nanosheets (endothermic reaction) than N_2 adsorption (exothermic reaction). As the temperature increases, the rate of adsorption of N_2 becomes larger than the rate of degradation of sodium cholate, resulting in the overall mass increase. The TGA curve for sodium cholate is shown in Fig. S25, ESI.† The DSC curve for TiB_2 nanosheets shows two endothermic peaks at ∼105 °C and ∼200 °C, indicating degradation of the surfactant. However, the overall curve represents exothermic reaction, indicating the adsorption of N_2 over nanosheets which results in the net mass gain. The mass of bulk TiB_2 remained practically constant with no change in color (Fig. 5b), in line with its inherent chemical inertness.

We performed further characterization on nanosheets recovered from TGA. The XRD pattern confirms that the native lattice structure of TiB_2 nanosheets was retained where the major planes (001), (100), and (101) were still present (Fig. S26, ESI†). We also found the presence of additional phases such as BN, TiN_xO_y, $TiBO_3$, and BNO. FTIR spectroscopy corroborated the phases that were observed in the XRD patterns (Fig. S27, ESI†). XPS studies further confirmed the presence of the Ti–B bond along with other bonds such as BN and TiN_xO_y (Fig. S28, ESI†).

To obtain further insights into the N_2 adsorption over TiB_2 nanosheets and the role played by defects/vacancies, we performed DFT calculations using an optimized 3 × 3 × 3 slab structure of the TiB_2 unit cell generated with 15 Å vacuum in the [0 0 1] direction (Fig. S29, ESI†). DFT simulations showed interesting results on the role played by defects in the ease of adsorption of N_2. With respect to the N_2 adsorption, specific defects were equivalent in terms of the lattice symmetry. Thus, there were 6 types of monovacant defects considered, namely T1 and T2 indicating vacancies in a Ti site and B1, B2, B3 and B4 indicating vacancies in B sites (Fig. S30, Tables S5 and S6, ESI†). In addition, a divacant site for boron was also considered, labelled B1B1, referring to two B vacancies in equivalent B1 sites.

It is to be noted that only monovacant Ti defects were considered, as Ti has higher affinity towards N_2

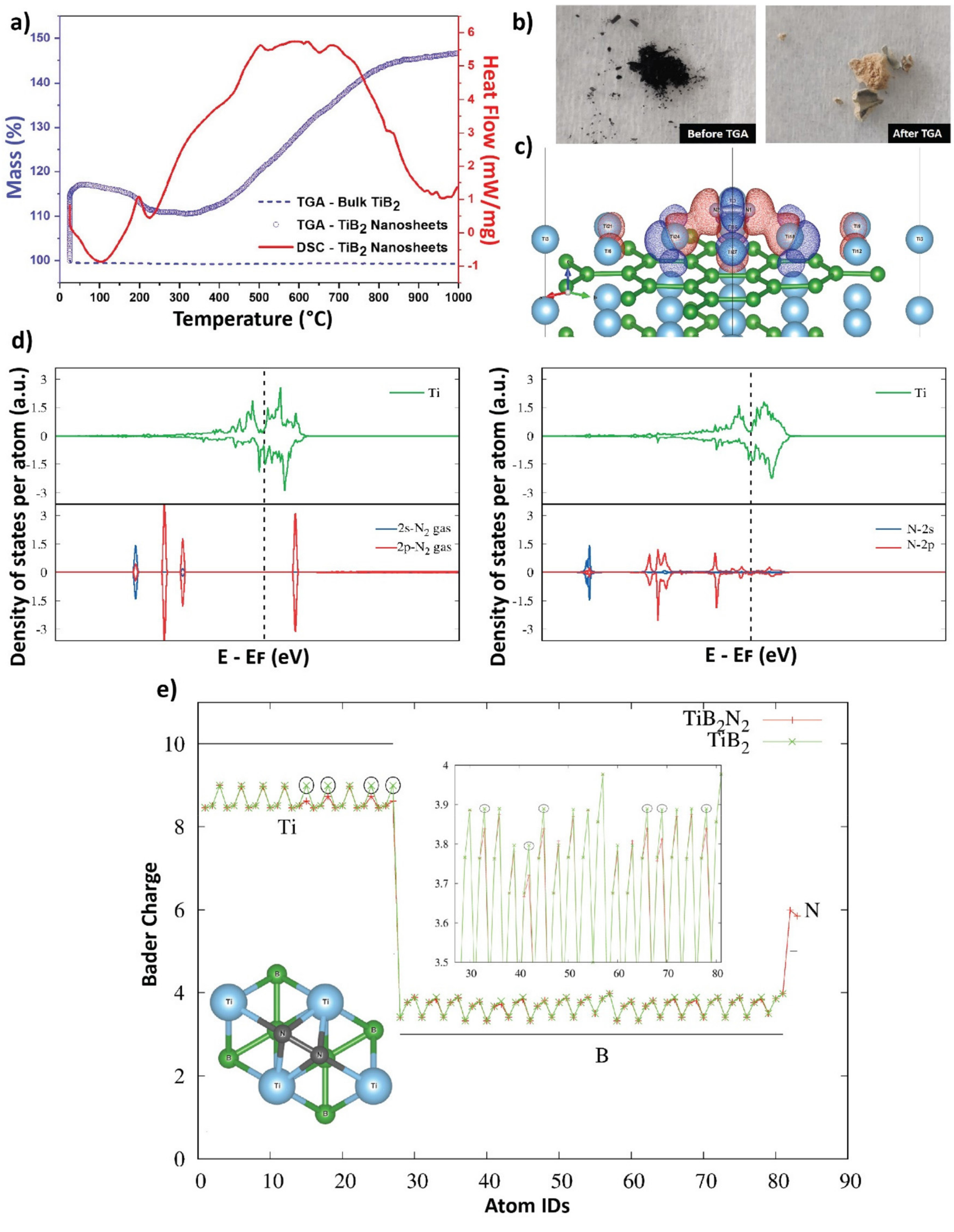

Fig. 5 Nitrogen adsorption under ambient conditions. (a) TGA plot for bulk TiB_2 and TGA–DSC plot for TiB_2 nanosheets indicating the propensity of TiB_2 nanosheets to chemisorb N_2, (b) optical image of TiB_2 nanosheets before and after TGA studies showing black and orange color respectively. (c) Charge density difference calculated for the case of pristine TiB_2 with N_2 adsorbed on the Ti-(0 0 1) surface using the optimized charge density of pristine TiB_2, N_2, and TiB_2N_2. After adsorption of N_2, the red area (positive) denotes the accumulation of charge and the blue areas (negative) denotes the depletion of charge. (d) Partial Density of States (PDOS) plots for pristine Ti and N_2 gas before adsorption (left) and after N_2 adsorption (right). (e) Bader charge analysis[79–82] of the TiB_2 and N_2 adsorbed TiB_2 structures. The final configuration of the adsorbed N_2 molecule is shown in the inset. Circles drawn around Ti atoms refer to the atom IDs of relevant atoms that contribute to the charge transfer in the N_2 adsorption process.

adsorption, whereas the role played by boron vacancies was to expose the Ti layer underneath for enhanced N_2 adsorption.

Initially, to understand the overall charge transfer process during the adsorption of N_2, we analysed the charge density distribution for three different systems, namely, pristine TiB_2

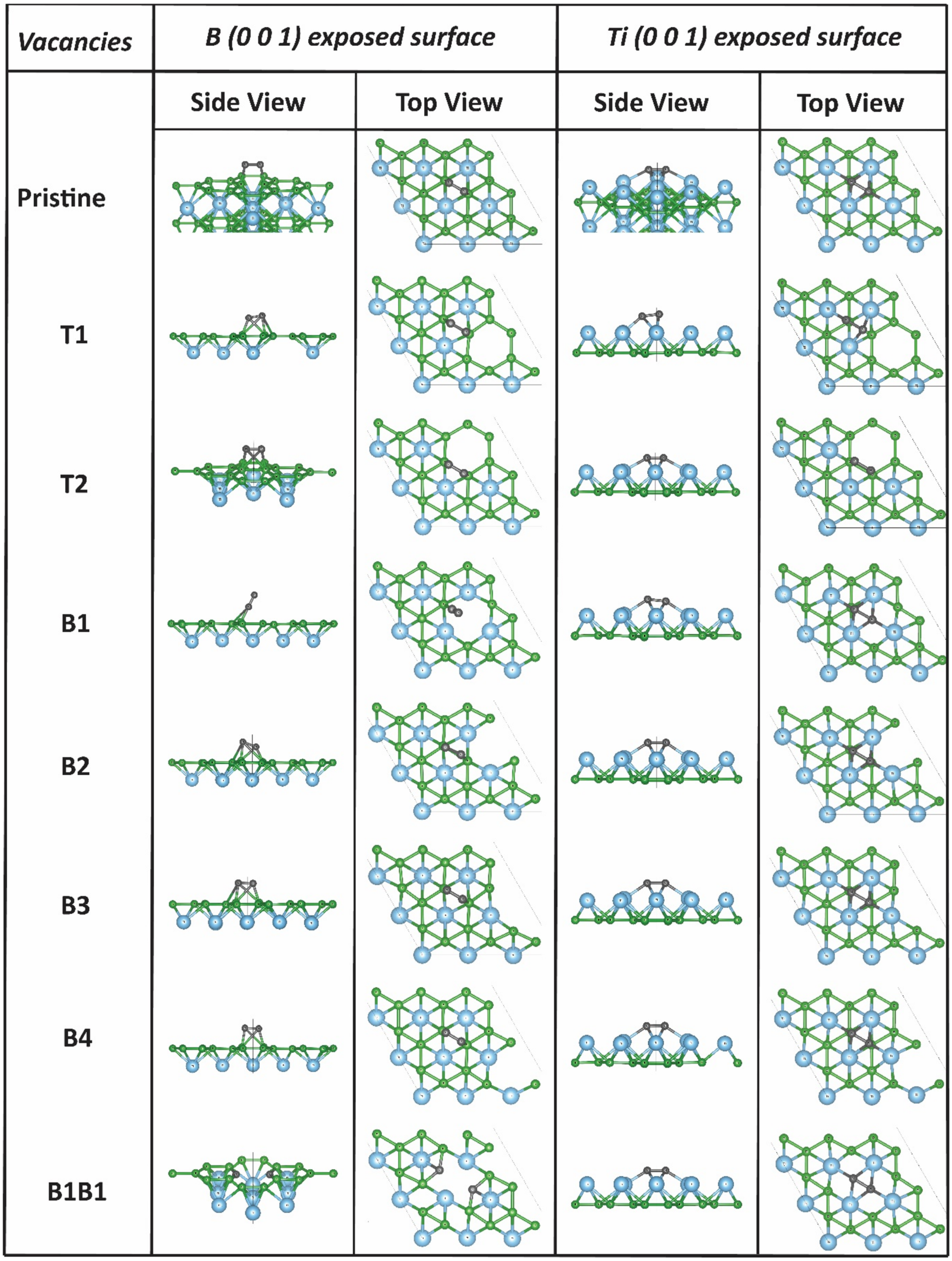

Fig. 6 Side view and top view of the final relaxed structures after N_2 adsorption for the B (0 0 1) – exposed surface and Ti (0 0 1) – exposed surface. Panels represent (a) pristine, (b) T1 vacancy, (c) T2 vacancy, (d) B1 vacancy, (e) B2 vacancy, (f) B3 vacancy, (g) B4 vacancy, and (h) B1B1 (divacancy). Divacant systems (B1B1) show the highest affinity for N_2 adsorption. Generally, a Ti-exposed layer has more affinity for N_2 adsorption than a B-exposed layer with the pristine B-exposed layer with no defects having the lowest affinity.

(with the Ti (0 0 1) surface exposed), a lone N_2 molecule, and N_2 adsorbed on TiB_2. The charge density difference plot (Fig. 5c) indicates charge depletion from the 4 Ti atoms underneath adsorbed N_2. We obtained the partial density of states (PDOS) plots before and after the N_2 adsorption on the TiB_2–Ti (0 0 1) surface (Fig. 5d). For Ti, we considered only the top surface atoms to calculate the total DOS – this revealed that there are less unoccupied states (right side of the dashed line). From the DOS plots for N, it's evident that the unoccupied states are now occupied after adsorption. The DOS plot for B exhibits negligible changes upon N_2 adsorption, and hence it is not shown here. Furthermore, we performed PDOS calculations for pristine TiB_2, N_2 gas, and N_2-adsorbed-TiB_2, and found that the unoccupied states of N_2 disappear after adsorption. Therefore, the primary role played by B is to expose the Ti surface for N_2 adsorption, mediated by the presence of defects.

Fig. 5e shows the Bader charges for various Ti, B and N atoms in the pristine TiB_2–N_2 system. The Bader charge analysis reveals that after the adsorption there is charge transfer from Ti and B atoms to nitrogen. The calculation setup considers Ti, B, and, N with 10, 3 and, 5 electrons respectively; after optimization the Bader charges shows that Ti donates electrons to B and N. The corresponding Bader charges are shown in Table S7, ESI.† The Bader charge analysis further indicates that 4 Ti atoms and 6 B atoms underneath the adsorbed N_2 molecule are actively involved in the charge transfer process.

We computed the adsorption energies of N_2 over various exposed surfaces (with and without defects, and with the Ti-exposed (0 0 1) and B-exposed (0 0 1) surfaces, Tables S7 and S8, ESI†). It was observed that the system with the most negative average adsorption energy was the divacant system for either case, where Ti (0 0 1) or B (0 0 1) is the exposed layer. Amongst the two surfaces, the B (0 0 1) surface with divacant B atoms ($TiB_{1.926}$–B1B1 system) showed the largest propensity for N_2 adsorption. This analysis indicates that the vacancy-rich TiB_2 nanosheets show an enhanced N_2 adsorption on the surface. The final ground state structures of all the surfaces (top view) after N_2 adsorption are shown in Fig. 6.

Finally, the two pristine surfaces (Ti and B exposed) and their boron divacant counterparts (showing maximum affinity for N_2 adsorption) were studied in order to get the average adsorption energies according to eqn (1) (presented in Table S8, ESI†). The results indicate that nanosheets with a Ti exposed layer have higher affinity for N_2 adsorption than those with a B exposed layer. Divacant systems with either a B-exposed layer or a Ti-exposed layer have the highest affinity for N_2 adsorption, while a configuration with a B-exposed layer with no defects has the least affinity. These findings complement the XPS results, where N_2 bonding was observed in both the B 1s and Ti 2p spectra of TiB_2 nanosheets, whereas only the Ti 2p spectra of bulk TiB_2 show N bonding.

The chemisorption of N_2 on the nanosheets opens up unprecedented opportunities to be utilized in various applications. The nanosheets could be used as a detector for N-based contaminants with excellent sensitivity and selectivity.[83] Moreover, the synergy of Ti and B can facilitate N_2 adsorption by accepting lone pair electrons from N_2 to d-orbitals as shown in Fig. 5d and N_2 activation by stabilizing intermediate species through charge modulation.[18,19,84] Thus, TiB_2 can act as an excellent catalyst for nitrogen reduction reaction. In addition, TiB_2 nanosheets after N_2 adsorption can potentially be used as an excellent H_2 storage material.[85]

Conclusion

We have demonstrated that a surfactant-based approach can be used to exfoliate TiB_2, a layered ionic material, in high yields with minimal functionalization. The implications of this study go beyond TiB_2 as this approach can be extended to exfoliate several other layered metal diborides while retaining their inherent structure. The surfactant concentration can be further used to tailor the stoichiometry of nanosheets based on specific applications. The counter-intuitive finding of N_2 chemisorption on these TiB_2 nanosheets under ambient conditions provides a sneak peek into the rich potential of quasi-2D metal diborides. DFT calculations elucidate the critical role played by vacancies and the Ti–B synergy in TiB_2 nanosheets for N_2 adsorption without requiring any energy input. It would be promising to study the reversibility of N_2 adsorption and the effect of external conditions in the future. The growing body of literature on metal boride nanostructures indicates that it would be promising to explore the candidacy of these nanosheets in energy generation and storage. We anticipate that this exfoliation approach will be a stepping stone to obtain quasi-2D forms of several other layered metal diborides for developing next-generation catalysts.

Conflicts of interest

The authors declare no competing results.

Acknowledgements

We would like to acknowledge the Central Instrumentation Facility of IIT Gandhinagar for providing various instrumental facilities. We also thank CRF – IIT Delhi for helping with Raman spectroscopy, SAIF – IIT Bombay for EPR spectroscopy, and AMRC – IIT Mandi for XPS analysis. KJ acknowledges the funding from the seed grant from the IITGN and the Core Research Grant (No. EMR/2017/000730) by the Department of Science and Technology India. KJ also acknowledges the funding from the Armament Research board (ARMREB/CDSW/2019/219) and funding provided by the Dr Dinesh O Shah Chair Fellowship. RR acknowledges the funding from the Indian Space Research Organization through the RESPOND program (Project # ISRO/RES/3/885/21-22). AT acknowledges funding through the IITGN Early Career Fellowship (Grant No.: MIS/IITGN/R&D/KJ/202122/028. The authors thank Asha Liza James for her constant motivation and providing useful insights. The authors also thank Bhagyashri Gaykwad for providing useful comments. The authors also thank chemical engineering office staff Mr Supresh, Mr Suvakanta, and Mr Rohit for their constant assistance in our day-to-day work.

References

1 K. S. Novoselov, A. K. Geim, S. v. Morozov, D. Jiang, Y. Zhang, S. v. Dubonos, I. v. Grigorieva and A. A. Firsov, *Science*, 2004, **306**, 666–669.
2 K. L. Marsh, M. Souliman and R. B. Kaner, *Chem. Commun.*, 2015, **51**, 187–190.
3 X. Nie, G. Li, Z. Jiang, W. Li, T. Ouyang and J. Wang, *Nanomaterials*, 2020, **10**, 1035.
4 A. Gupta and S. Vasudevan, *J. Phys. Chem. C*, 2018, **122**, 19243–19250.
5 R. J. Smith, P. J. King, M. Lotya, C. Wirtz, U. Khan, S. De, A. O'Neill, G. S. Duesberg, J. C. Grunlan, G. Moriarty, J. Chen, J. Wang, A. I. Minett, V. Nicolosi and J. N. Coleman, *Adv. Mater.*, 2011, **23**, 3944–3948.
6 F. Feng, H. Guo, D. Li, C. Wu, J. Wu, W. Zhang, S. Fan, Y. Yang, X. Wu, J. Yang, B. Ye and Y. Xie, *ACS Nano*, 2015, **9**, 1683–1691.
7 J.-U. Lee, S. Lee, J. Hoon Ryoo, S. Kang, T. Yun Kim, P. Kim, C.-H. Park, J.-G. Park and H. Cheong, *Nano Lett.*, 2016, **16**, 7433–7438.
8 Y. Gogotsi and B. Anasori, *ACS Nano*, 2019, **13**, 8491–8494.
9 S. Kartik Nemani, B. Zhang, B. C. Wyatt, Z. D. Hood, S. Manna, R. Khaledialidusti, W. Hong, M. G. Sternberg, S. K. R. S. Sankaranarayanan and B. Anasori, *ACS Nano*, 2021, **15**, 12815–12825.
10 R. W. McKinney, P. Gorai, S. Manna, E. Toberer and V. Stevanović, *J. Mater. Chem. A*, 2018, **6**, 15828–15838.
11 H. Yi, S. Liu, C. Lai, G. Zeng, M. Li, X. Liu, B. Li, X. Huo, L. Qin, L. Li, M. Zhang, Y. Fu, Z. An and L. Chen, *Adv. Energy Mater.*, 2021, **11**, 2002863.
12 J. Mee Lee, B. Kang, Y. Kyung Jo and S.-J. Hwang, *ACS Appl. Mater. Interfaces*, 2019, **11**, 12121–12132.
13 Y. Fu, P. Richardson, K. Li, H. Yu, B. Yu, S. Donne, E. Kisi and T. Ma, *Nano-Micro Lett.*, 2020, **12**, 1–13.
14 B. Zhang, J. Zhou and Z. Sun, *J. Mater. Chem. A*, 2022, **10**, 15865–15880.
15 J. K. Burdett, E. Canadell and G. J. Miller, *J. Am. Chem. Soc.*, 2002, **108**, 6561–6568.
16 J. Nagamatsu, N. Nakagawa, T. Muranaka, Y. Zenitani and J. Akimitsu, *Nature*, 2001, **410**, 63–64.
17 N. Gupta, B. Basu, V. V. B. Prasad and M. Vemuri, *Def. Sci. J.*, 2012, **62**, 382–389.
18 Y. Shi, S. Xu and F. Li, *Chem. Commun.*, 2022, **58**, 8714–8717.
19 H. Y. Zhou, Y. bin Qu, J. C. Li, Z. L. Wang, C. C. Yang and Q. Jiang, *Appl. Catal., B*, 2022, **305**, 121023.
20 S. K. Das, A. Bedar, A. Kannan and K. Jasuja, *Sci. Rep.*, 2015, **5**, 1–11.
21 A. L. James and K. Jasuja, *RSC Adv.*, 2017, **7**, 1905–1914.
22 R. Saraswat, A. L. James and K. Jasuja, *Adv. Appl. Ceram.*, 2019, **118**, 209–216.
23 H. Gunda, S. K. Das and K. Jasuja, *ChemPhysChem*, 2018, **19**, 880–891.
24 H. Nishino, T. Fujita, N. T. Cuong, S. Tominaka, M. Miyauchi, S. Iimura, A. Hirata, N. Umezawa, S. Okada, E. Nishibori, A. Fujino, T. Fujimori, S. Ito, J. Nakamura, H. Hosono and T. Kondo, *J. Am. Chem. Soc.*, 2017, **139**, 13761–13769.
25 S. K. Das and K. Jasuja, *ACS Appl. Nano Mater.*, 2018, **1**, 1612–1622.
26 D. Ratnam, S. K. Das and K. Jasuja, *IOP Conf. Ser.: Mater. Sci. Eng.*, 2017, **225**, 12111.
27 A. Yousaf, M. S. Gilliam, S. L. Y. Chang, M. Augustin, Y. Guo, F. Tahir, M. Wang, A. Schwindt, X. S. Chu, D. O. Li, S. Kale, A. Debnath, Y. Liu, M. D. Green, E. J. G. Santos, A. A. Green and Q. H. Wang, *J. Phys. Chem. C*, 2021, **125**, 6787–6799.
28 H. Gunda, C. Ghoroi and K. Jasuja, *Thermochim. Acta*, 2020, **690**, 178674.
29 Y.-S. Liu, K. G. Ray, M. Jørgensen, T. M. Mattox, D. F. Cowgill, H. Eshelman, A. M. Sawvel, J. L. Snider, W. York, P. Wijeratne, A. Pham, G. Harini, S. Li, T. W. Heo, S. Kang, T. R. Jensen, V. Stavila, B. C. Wood and L. E. Klebanoff, *J. Phys. Chem. C*, 2020, **39**, 21761–21771.
30 G. Akopov, L. E. Pangilinan, R. Mohammadi and R. B. Kaner, *APL Mater.*, 2018, **6**, 70901.
31 C. S. Lim, Z. Sofer, V. Mazánek and M. Pumera, *Nanoscale*, 2015, **7**, 12527–12534.
32 S. K. John and A. A. Anappara, *New J. Chem.*, 2019, **43**, 9953–9960.
33 A. L. James, M. Lenka, N. Pandey, A. Ojha, A. Kumar, R. Saraswat, P. Thareja, V. Krishnan and K. Jasuja, *Nanoscale*, 2020, **12**, 17121–17131.
34 V. Jani, A. Rasyotra, H. Gunda, C. Ghoroi and K. Jasuja, *Ceram. Int.*, 2022, **48**, 32380–32388.
35 A. Varma, R. Badam, A. L. James, K. Higashimine, K. Jasuja and N. Matsumi, *ACS Appl. Nano Mater.*, 2022, **5**, 16154–16163.
36 S. Suriyakumar, A. Varma, V. Surendran, K. Jasuja and M. M. Shaijumon, *Batteries Supercaps*, 2022, **5**, e202100243.
37 G. Joshi, S. Chakrabarty, S. Khatua and K. Jasuja, *Int. J. Hydrogen Energy*, 2022, DOI: 10.1016/j.ijhydene.2022.07.232.
38 B. F. MacHado and P. Serp, *Catal. Sci. Technol.*, 2011, **2**, 54–75.
39 S. K. Das, R. Gawas, S. Chakrabarty, G. Harini, R. Patidar and K. Jasuja, *J. Phys. Chem. C*, 2019, **123**, 25412–25421.
40 R. Patidar, H. Gunda, A. K. Varma, R. Gawas, S. K. Das and K. Jasuja, *Ceram. Int.*, 2020, **46**, 28324–28331.
41 A. Griffin, K. Nisi, J. Pepper, A. Harvey, B. M. Szydłowska, J. N. Coleman and C. Backes, *Chem. Mater.*, 2020, **32**, 2852–2862.
42 G. Kresse and J. Hafner, *Phys. Rev. B: Condens. Matter Mater. Phys.*, 1993, **47**, 558–561.
43 G. Kresse and J. Furthmüller, *Comput. Mater. Sci.*, 1996, **6**, 15–50.

44 G. Kresse and J. Furthmüller, *Phys. Rev. B: Condens. Matter Mater. Phys.*, 1996, **54**, 11169–11186.
45 J. P. Perdew, K. Burke and M. Ernzerhof, *Phys. Rev. Lett.*, 1996, **77**, 3865–3868.
46 S. Grimme, *J. Comput. Chem.*, 2006, **27**, 1787–1799.
47 P. Ramalingam, S. T. Pusuluri, S. Periasamy, R. Veerabahu and J. Kulandaivel, *RSC Adv.*, 2013, **3**, 2369–2378.
48 Y. J. Lee, L. Huang, H. Wang, M. L. Sushko, B. Schwenzer, I. A. Aksay and J. Liu, *Colloids Interface Sci. Commun.*, 2015, **8**, 1–5.
49 R. v. Gorbachev, I. Riaz, R. R. Nair, R. Jalil, L. Britnell, B. D. Belle, E. W. Hill, K. S. Novoselov, K. Watanabe, T. Taniguchi, A. K. Geim and P. Blake, *Small*, 2011, **7**, 465–468.
50 J. N. Coleman, M. Lotya, A. O'Neill, S. D. Bergin, P. J. King, U. Khan, K. Young, A. Gaucher, S. De, R. J. Smith, I. v Shvets, S. K. Arora, G. Stanton, H.-Y. Kim, K. Lee, G. T. Kim, G. S. Duesberg, T. Hallam, J. J. Boland, J. J. Wang, J. F. Donegan, J. C. Grunlan, G. Moriarty, A. Shmeliov, R. J. Nicholls, J. M. Perkins, E. M. Grieveson, K. Theuwissen, D. W. McComb, P. D. Nellist and V. Nicolosi, *Science*, 2011, **331**, 568 LP–568571.
51 Y. Lin, T. v Williams, T.-B. Xu, W. Cao, H. E. Elsayed-Ali and J. W. Connell, *J. Phys. Chem. C*, 2011, **115**, 2679–2685.
52 M. Naguib, O. Mashtalir, J. Carle, V. Presser, J. Lu, L. Hultman, Y. Gogotsi and M. W. Barsoum, *ACS Nano*, 2012, **6**, 1322–1331.
53 C. F. Holder and R. E. Schaak, *ACS Nano*, 2019, **13**, 7359–7365.
54 V. Mazánek, H. Nahdi, J. Luxa, Z. Sofer and M. Pumera, *Nanoscale*, 2018, **10**, 11544–11552.
55 S. M. Sichkar, V. N. Antonov and V. P. Antropov, *Phys. Rev. B: Condens. Matter Mater. Phys.*, 2013, **87**, 064305.
56 U. D. Wdowik, A. Twardowska and B. Rajchel, *Adv. Condens. Matter Phys.*, 2017, **2017**, 4207301.
57 G. M. National Institute of Standards and Technology, NIST X-ray Photoelectron Spectroscopy Database, NIST Standard Reference Database Number 20.
58 C. Backes, T. M. Higgins, A. Kelly, C. Boland, A. Harvey, D. Hanlon and J. N. Coleman, *Chem. Mater.*, 2017, **29**, 243–255.
59 L. J. Ji, Y. Qin, D. Gui, W. Li, Y. Li, X. Li and P. Lu, *Chem. Mater.*, 2018, **30**, 8732–8738.
60 Y. Han, Y. Dai, D. Shu, J. Wang and B. Sun, *J. Alloys Compd.*, 2007, **438**, 327–331.
61 M. Xin-min, X. Rui-juan, W. Hao and W. Wei-min, *J. Wuhan Univ. Technol., Mater. Sci. Ed.*, 2003, **18**, 11–14.
62 S. Li, H. Gunda, K. G. Ray, C.-S. Wong, P. Xiao, R. W. Friddle, Y.-S. Liu, S. Kang, C. Dun, J. D. Sugar, R. D. Kolasinski, L. F. Wan, A. A. Baker, J. R. I. Lee, J. J. Urban, K. Jasuja, M. D. Allendorf, V. Stavila and B. C. Wood, *Nat. Commun.*, 2021, **12**, 6268.
63 S. Chakrabarty, A. Thakur, A. Rasyotra, B. Gaykwad and K. Jasuja, *J. Phys. Chem. C*, 2023, **127**, 852–870.
64 I. R. Shein, N. I. Medvedeva and A. L. Ivanovskii, *Phys. Solid State*, 2003, **45**, 1617–1621.
65 H. Zhang and R. Lv, *J. Materiomics*, 2018, **4**, 95–107.
66 T. Skaltsas, X. Ke, C. Bittencourt and N. Tagmatarchis, *J. Phys. Chem. C*, 2013, **117**, 23272–23278.
67 Z. Li, R. J. Young, C. Backes, W. Zhao, X. Zhang, A. A. Zhukov, E. Tillotson, A. P. Conlan, F. Ding, S. J. Haigh, K. S. Novoselov and J. N. Coleman, *ACS Nano*, 2020, **14**, 10976–10985.
68 G. Greczynski and L. Hultman, *J. Appl. Phys.*, 2022, **132**, 011101.
69 G. R. Panghulan, M. R. Vasquez, Y. D. Edañol, N. Chanlek and L. M. Payawan, *J. Vac. Sci. Technol., B: Nanotechnol. Microelectron.: Mater., Process., Meas., Phenom.*, 2020, **38**, 062203.
70 J. F. Moulder and C. Jill, *Handbook of X-ray photoelectron spectroscopy: a reference book of standard spectra for identification and interpretation of XPS data*, Physical Electronics Division, Perkin-Elmer Corp., Eden Prairie, Minn., 1992.
71 S. P. Gordienko, *Powder Metall. Met. Ceram.*, 2003, **42**, 287–290.
72 A. Hinckley and A. Muscat, *Solid State Phenomena*, 2018, **282**, 232–237.
73 S. Jiang, B. Yi, H. Zhang, W. Song, Y. Bai, H. Yu and Z. Shao, *ChemElectroChem*, 2016, **3**, 734–740.
74 Y. Han, X. Yue, Y. Jin, X. Huang and P. K. Shen, *J. Mater. Chem. A*, 2016, **4**, 3673–3677.
75 E. O. Filatova, S. S. Sakhonenkov, A. S. Konashuk, S. A. Kasatikov and V. V. Afanas'Ev, *J. Phys. Chem. C*, 2019, **123**, 22335–22344.
76 D. Choi and P. N. Kumta, *J. Electrochem. Soc.*, 2006, **153**, A2298.
77 T. Shen, S. Liu, W. Yan and J. Wang, *J. Mater. Sci.*, 2019, **54**, 8852–8859.
78 Q. Liu, C. Chen, M. Du, Y. Wu, C. Ren, K. Ding, M. Song and C. Huang, *ACS Appl. Nano Mater.*, 2018, **1**, 4566–4575.
79 M. Yu and D. R. Trinkle, *J. Chem. Phys.*, 2011, **134**, 064111.
80 G. Henkelman, A. Arnaldsson and H. Jónsson, *Comput. Mater. Sci.*, 2006, **36**, 354–360.
81 E. Sanville, S. D. Kenny, R. Smith and G. Henkelman, *J. Comput. Chem.*, 2007, **28**, 899–908.
82 W. Tang, E. Sanville and G. Henkelman, *J. Phys.: Condens. Matter*, 2009, **21**, 084204.
83 T. Chen, Z. Cheng, Q. Tian, J. Wang, X. Yu and D. Ho, *ACS Appl. Nano Mater.*, 2020, **3**, 6440–6447.
84 S. Li, Y. Wang, J. Liang, T. Xu, D. Ma, Q. Liu, T. Li, S. Xu, G. Chen, A. M. Asiri, Y. Luo, Q. Wu and X. Sun, *Mater. Today Phys.*, 2021, **18**, 100396.
85 K. E. Lamb, M. D. Dolan and D. F. Kennedy, *Int. J. Hydrogen Energy*, 2019, **44**, 3580–3593.

